Structure and Dielectric Studies of Sn^{4+}/Er^{3+} co-doped $BaTiO_3$ Nano-Powders

R. Mahani[a,*], O. El-Sayed[b], S.K. El-Mahy[b] and I.K. Battisha[c]

[a]Microwave Physics and Dielectrics Dept., National Research Centre, 33 El Bohouth Str., 12622 Giza, Egypt

[b]Physics Department, Faculty of Women for Arts, Science and Education, Ain Shams University, Cairo, Egypt

[c]Solid State Physics Dept., National Research Centre, 33 El Bohouth Str., 12622 Giza, Egypt

(Received November 27, 2019; revised version December 23, 2019; in final form December 24, 2019)

Nanocrystalline barium titanate (BTO_3) powders annealed at 1050 °C for 4 h, were synthesized using the sol–gel method and the effects of Sn^{4+}/Er^{3+} co-doping ($BTSO_3$:2Er) on microstructure and dielectric properties of BTO_3 powders, were investigated. The crystalline structure, microstructure, molecular structure, and dielectric properties were investigated using X-ray powder diffraction, field emission scanning electron microscope, with energy dispersive X-ray analysis, the Fourier transform infra-red spectroscopy, and dielectric spectrometer. X-ray powder diffraction analysis confirmed the formation of both BTO_3 and $BTSO_3$:2Er in a single tetragonal phase. For $BTSO_3$:2Er sample, the particle size decreased from 64 for pure BTO_3 to 57.11 nm for $BTSO_3$:2Er, inhibiting grain growth upon co-doping with Sn^{4+}/Er^{3+} ions. Further, according to field emission scanning electron microscope observations, the Fourier transform infra-red spectroscopy analysis showed a new band assigned to M–O. Correspondingly, $BTSO_3$:2Er showed an anomaly relaxation peak whose maximum was positioned at temperature value (174 °C) higher than the Curie temperature (T_C) according to permittivity measurements. Its T_C shifted from 125 to 103 °C and permittivity considerably increased to become ten times greater than that of pure BTO_3, revealing enhancements of dielectric properties upon doping with Sn^{4+}/Er^{3+} ions. Also, AC conductivity for $BTSO_3$:2Er sample considerably increased due to the formation of excess oxygen vacancies.

DOI: 10.12693/APhysPolA.137.410

PACS/topics: nanopowder, X-ray diffraction, barium titanate, dielectric properties

1. Introduction

Barium titanate (BTO_3) has been considered as one of the ferroelectric materials most frequently used in manufacturing various microelectronic devices due to its unique electrical properties, mechanical and chemical stability [1]. Much attention has been paid to prepare such ceramics with an average grain size below 100 nm to improve their electrical properties to be used in fabricating multilayer ceramic capacitors (MLCCs) with high efficiency. However, MLCCs based BTO_3 have still some drawbacks originating from the degradation of ferroelectric and dielectric properties when the grain size decreases [2]. Many attempts were made to overcome such problems and to prepare BTO_3 sample with fine particle size, controlled stoichiometry, and uniformity. Currently, there are two methods for synthesizing BTO_3 sample: solid-phase [3] and liquid-phase methods [4]. The traditional solid phase method of high sintering temperatures still has some drawbacks such as serious agglomeration and coarse grains. Instead, the sol–gel method of low sintering temperature provides a new approach to the preparation of high purity, uniform, and ultrafine metal oxide nanoparticles in a few steps [2]. Thus, in the current study, the sol–gel method has been used to prepare pure (BTO_3) and Sn^{4+}/Er^{3+} co-doped barium titanate ($BTSO_3$:2Er) nanopowders.

*corresponding author; e-mail: rmsoliman66@yahoo.com

The doping mechanism and influence of the large rare-earth ions on structural and electrical properties of BTO_3 ceramics have been extensively studied [5, 6]. By definition, the relaxor ferroelectrics are well characterized by broad relaxation peaks in their dielectric spectra which shifted to higher temperatures with increasing frequency [7, 8]. The relaxor phenomenon was first evidenced in $Ba(Ti_{1-x}\text{-}Sn_x)O_3$, and is currently ascribed to the development of polar nanoregions (PNRs) [9, 10]. On the other hand, the polarized domains in pure $BaTiO_3$ exhibit a sharp relaxation peak at the phase transition temperature, i.e. the Curie temperature ($T_C \sim 130$ °C) [11]. Several types of research reported a diffused phase transition in $Ba(Ti_{0.7}Sn_{0.3})O_3$ that achieves complete relaxor characteristics [12]. This results in increase of permittivity, tunability under biasing field, as well as a reduction of the low-frequency dielectric losses. The addition of rare-earth (RE^{3+}) elements to BTO_3 was found to be useful for producing semiconducting materials which in turn enables the development of positive temperature coefficient resistors (PTCR) [13]. The special interest is given for rare-earth cations because some of them exhibit amphoteric behavior when they incorporated into the BTO_3 structure. For instance, lanthanide ions from Sm^{3+} to Er^{3+}, having a particle size between Ba^{2+} and Ti^{4+}, can be accommodated either at A or B lattice sites, depending on their concentrations and stoichiometry of the hosting structure [12, 14, 15]. Erbium (Er^{3+}) has been widely used because of its great technological interest [16]. As its particle size (0.89 Å) value lies between Ba^{2+} (1.61 Å) and Ti^{4+} (0.605 Å),

it would occupy Ti-site to improve the stability of BTO_3 at this location [17, 18]. Based on the above, the main objective of the current study is to investigate two subjects BTO_3 and $BTSO_3$:2Er. The first is to prepare these ceramics on the nanoscale having sufficiently high permittivity to be useful for electrical capacitors and relaxors fabrication. The second concerns the effect of Sn^{4+}/Er^{3+} co-doping on their microstructure, crystalline structure, and dielectric properties. Sample's structure was characterized using X-ray diffraction (XRD) and field emission scanning electron microscopy (FESEM) whereas their dielectric properties were studied over a temperature range (-50 °C to 200 °C) at different frequencies.

2. Materials and methods

2.1. Synthesis procedure

The chemical starting materials used in the present study were barium acetate $Ba(CH_3COO)_2$ (Aldrich 99%), titanium(IV) *n*-butoxide $Ti(OC_4H_9)_4$ (Alfa Aesar 99+%). 35 ml acetyl acetone $C_5H_8O_2$ (Aldrich 99+%) and 20 ml acetic acid ($C_2H_4O_2$) diluted with distilled water (HAc)-H_2O were selected as solvents of 6.662 g titanium(IV) *n*-butoxide and 5 g barium acetate, respectively. Barium titanate (BTO_3) was obtained by reacting to two solutions of barium acetate and titanium(IV) *n*-butoxide (Sol 1) for 1 h on the stirrer. To obtain $BTSO_3$:2Er $\left(BaTi_{0.88}Sn_{0.1}Er_{0.02}O_3\right)$ Sol 1 was mixed with tin solution $\left(10\text{ mol.\% } SnCl_4 \cdot 5H_2O\right.$ (Strem Chemicals, Incorporated), dissolved in 16 ml isopropanol$\left.\right)$ for 15 min on the stirrer (Sol 2), and then added erbium solution (2 mol.% $Er(NO_3)_3{\cdot}5H_2O$ (Aldrich 99+%) dissolved in 5 ml distilled water), and then the mixture was stirred on hotplate for 50 min (Sol 3). As a result, gel was formed at 130 °C which was then annealed in air for 4 h at 1050 °C (using Muffle furnace type Carbolite CWF1200) and finally small crystallized samples of BTO_3 and $BTSO_3$:2Er were obtained.

For dielectric measurements, the fine ceramic sample was pressed into samples-shaped pellets having a diameter of 10 mm and a thickness of 2.4 mm under pressure of 40 MPa at room temperature. Then, both surfaces of each sample were coated with a silver paste to ensure good contacting.

2.2. Characterization of nanopowders

To examine the crystal structure of BTO_3 and $BTSO_3$:2Er nanopowders, XRD measurements were performed. Philips X-ray diffractometer having monochromatized Cu $K_{\alpha 1}$ ($\lambda = 1.5406$ Å) of power 40 kV × 30 mA, was used. The crystallite size (G) was calculated from the Scherrer equation [19]:

$$G = \frac{K\lambda}{D\cos(\theta)}, \tag{1}$$

where $K = 0.89$ is the Scherrer constant, λ is the wavelength, D is the full width (in radians) of the peak at half maximum (FWHM) intensity, and θ is the diffracted angle. FESEM together with energy dispersive X-ray (EDX) analysis were provided with a variable pressure FESEM instrument (FEI, model: Quanta 250 FEG) to determine the crystalline phases and elements. To achieve this, the samples were gold-sputtered using Edwards S150A Sputter coater to make the images more obvious. The sample's chemical structure was characterized using the Fourier transform infra-red spectroscopy using Thermo Nicolet, FT-IR, and NEXUS in the range from 400 up to 4000 cm^{-1}.

The dielectric measurements were carried out by inserting the sample between two conducting parallel plates forming a capacitor. The sample temperature was controlled by thermometer contact to the sample and temperature controller. A computerized Impedance Analyzer IM3570 was used to measure the dielectric properties of the prepared samples at a temperature range between (−50 and 200 °C) over a wide frequency range from 10^2 up to 10^6 Hz. The permittivity ε' and AC conductivity σ_{AC} were calculated from the output parameters like capacitance C and loss tangent $\tan(\delta)$ as follows:

$$\varepsilon' = \frac{Cd}{\varepsilon_0 A}, \tag{2}$$

$$\sigma_{AC} = \omega\varepsilon_0\varepsilon'\tan(\delta), \tag{3}$$

where ε_0 is the permittivity of free space (8.854×10^{-12} F/m), d is the sample thickness, and A is the sample surface area. The measurement uncertainty reported to be ±1% and ±3% in ε' and $\tan(\delta)$, respectively. The measurement reproducibility was tested by re-measuring ε' and $\tan(\delta)$ after experimenting once again.

3. Results and discussion

3.1. Structure and morphology study

Figure 1 illustrates XRD patterns for BTO_3 and $BTSO_3$:2Er powders annealed in air at 1050 °C for 4 h. It can be seen that all the observed peaks corresponding to BTO_3 tetragonal perovskite structure were presented in all patterns according to ICDD number [74-2491]. It is evident that the BTSO:2Er sample contains traces of SnO_2 without secondary phases results from Er^{3+} doping; referring to Er^{3+} nominally substitute for Ti^{4+} site and well soluble in host material due to its lower concentration. In $BTSO_3$:2Er, a preferential substitution Er^{3+} for B sites is postulated in $0 \leq Er^{3+} \leq 0.03$ composition range as well as the non-total stabilization of these parameters for $0.03 \leq Er^{3+} \leq 0.30$ [20]. Figure 1b shows the expanding area between $2\theta = 40°$ and $2\theta = 49°$ for both samples, which highlighted the splitting of (002) and (200) orientations at around 45° in 2θ scale, exploring the tetragonal feature for BTO_3 [21]. The splitting taken as 2θ distance between the peaks is large enough to confirm tetragonality for BTO_3 whereas it decreased for $BTSO_3$:2Er, referring to tetragonality decrease as confirmed by the calculations listed in Table I.

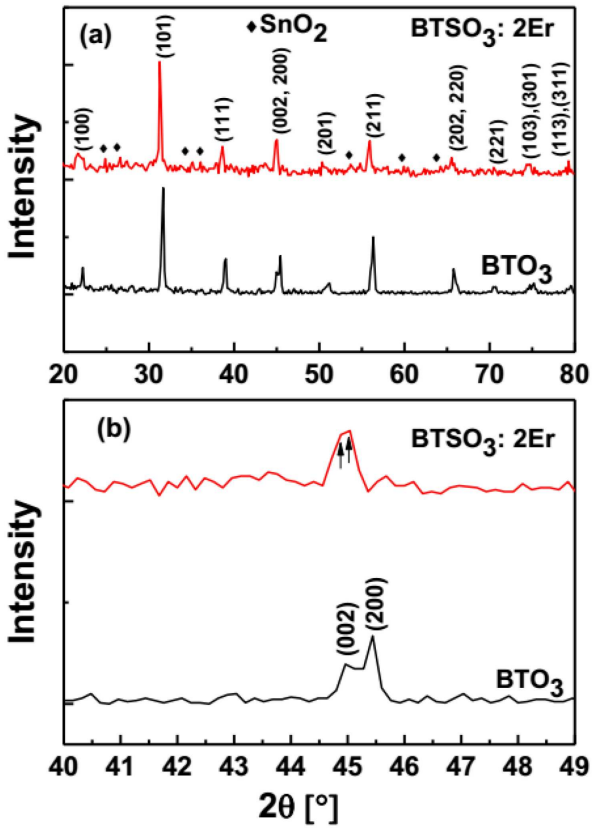

Fig. 1. XRD patterns of nano-crystalline BTO_3 and $BTSO_3$:2Er samples sintered in air for 4 h at 1050 °C (a), and those for expanding area between $2\theta = 44°$ and 46° (b).

TABLE I

Calculated crystallite size (CS), lattice parameters (a, c), and tetragonal factor (c/a) for BTO_3 and $BTSO_3$:2Er

Samples	CS [nm]	a [Å]	c [Å]	c/a
BTO_3	64	3.9888	4.020	1.0078
$BTSO_3$: 2Er	57.11	4.0000	4.0052	1.0013

To calculate the tetragonality factor, the lattice parameters (a, c) should be calculated at first from the following equation:

$$d_{hkl} = \frac{a}{\sqrt{h^2 + k^2 + \left(\frac{a}{c}\right)^2 l^2}}, \quad (4)$$

where d_{hkl} is the d-spacing for the (hkl) plane. Table I shows the crystallite sizes, lattice parameters (a, c) and tetragonal factor for BTO_3 and $BTSO_3$:2Er using the planes (200) and (002). The average crystallite size was found to be 64 and 57.11 nm for BTO_3 and $BTSO_3$:2Er, respectively, confirming that the samples were successfully prepared in the nanoscale.

FESEM microphotographs and the corresponding EDX images for BTO_3 and $BTSO_3$:2Er samples, are together illustrated in Figs. 2 and 3. It turns out that both

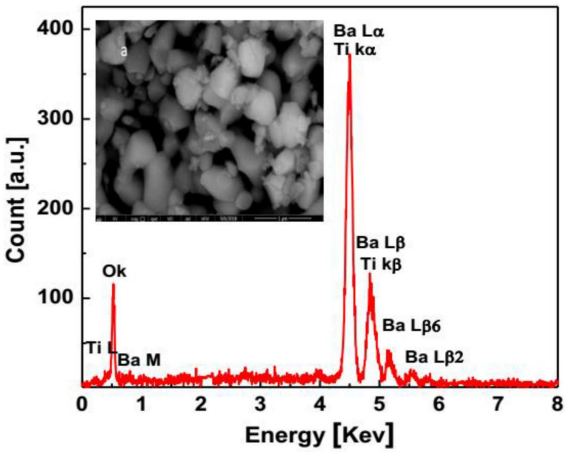

Fig. 2. FESEM/EDX image for BTO_3 sintered in air for 4 h at 1050 °C.

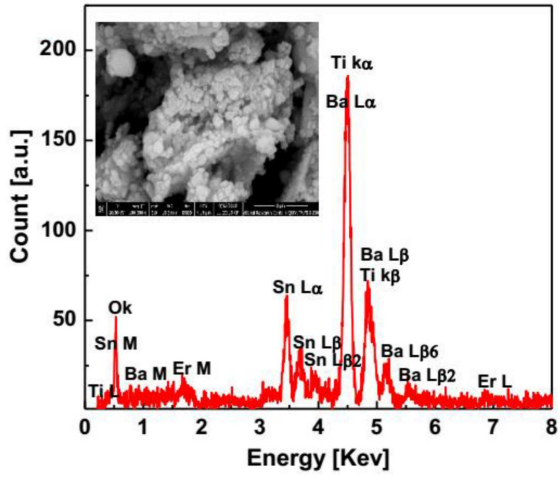

Fig. 3. FESEM/EDX image for $BTSO_3$:2Er sintered in air for 4 h at 1050 °C.

samples show free uniform grains. Inset of Fig. 3 and Table I show that the compensation mode of Sn^{4+}/Er^{3+} ions in $BaTiO_3$ can suppress grain growth, forming a uniform and fine-grained microstructure with an average grain size of 57.11 nm. Further, the surface morphology of $BTSO_3$:2Er shows different microstructure features due to doping with Sn^{4+} and Er^{4+} ions which have larger ionic radii than Ti^{4+}. Accordingly, $BTSO_3$:2Er has higher densification than pure BTO_3. To identify the purity of nanoparticle samples, dispersive X-ray analysis (EDX) is investigated. BTO_3 has high-intensity peaks corresponding to oxygen, Ba, and Ti elements, confirming the absence of any impurities. Similar peaks with lower intensities and additional peaks corresponding to Sn and Er elements are noticed for $BTSO_3$:2Er sample (Fig. 3).

FTIR spectra for BTO_3 and $BTSO_3$:2Er samples, are shown in Fig. 4. For BTO_3 spectra, the weak band at 549 cm^{-1} is assigned to M–O stretching vibration of

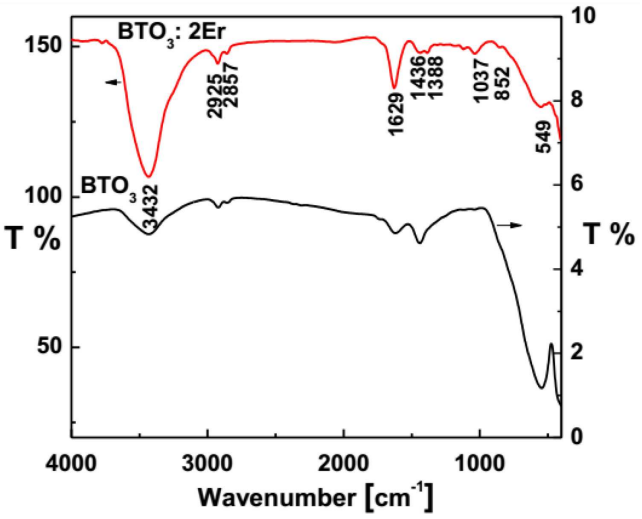

Fig. 4. FTIR spectra of BTO_3 and $BTSO_3$:2Er sintered in air for 4 h at 1050 °C.

TABLE II

Assignment for FTIR data of BTO_3 and $BTSO_3$:2Er

No.	Frequency [cm^{-1}]	Band assignment
1	549	T–O stretching vibration
2	852	Ti–O or Sn–O or Er–O stretching vibration
3	1037	CO_3^{2-} bending vibration
4	1388, 1436	CO_3^{2-}stretching vibration
5	1629	O–H bending vibration
6	2857	C–H stretching vibrations (CH_2 group)
7	2925	C–H stretching vibrations (CH_3 group)
8	3432	O–H stretching vibration

octahedral TiO_6 [22–24], whereas the band at 1436 cm^{-1} is assigned to lattice carbonate [25]. However, the last band has no evidence in XRD spectra due to the smaller particle size of lattice carbonate than the Bragg size, exploring more sensitivity of FTIR than XRD technique. The band at 1629 cm^{-1} is assigned to the O–H decomposition mode of absorbed water molecules and attributed to the bending vibration. The bands at 2925 and 2857 cm^{-1} are assigned to the CH_3 symmetric and CH_2 symmetric stretching C–H vibrations, respectively [26, 27]. The broad low-intensity band appearing at 3432 cm^{-1} is assigned to O–H stretching modes of surface adsorbed water. It describes the stretching vibration of weakly bound water interacting via hydrogen bond with its environment and also to stretching vibrations of hydrogen-bonded of OH-groups [28, 29].

FTIR spectra for $BTSO_3$:2Er sample shows all previous bands with extra two bands as listed in Table II. One band at 852 cm^{-1} is assigned to M–O stretching vibration that results from tetrahedral sites and oxygen complexes [14] due to co-doping, whereas the second band at 1037 cm^{-1} is assigned to CO_3^{2-} bending vibration. Further, there is a coexistence of OH stretching (at 3432 cm^{-1}) with the carbonate at 1037 and 1386 cm^{-1}, suggesting that carbonate would exist as hydroxycarbonate. Extensive work is needed to validate this point and to evaluate the possible reactions with air after annealing (and before FTIR experiments) which may contribute to carbonate and OH group [30]. This reaction is more active for the co-doped sample appearing as a strong band at 3432 cm^{-1} and additional carbonate bands.

3.2. Dielectric study

The dielectric studies for BTO_3 and $BTSO_3$:2Er sample included two parts. The first study involved the effect of temperature and frequency on permittivity (ε'). The second study was concerned with the frequency and temperature dependences of AC conductivity (σ_{AC}).

3.2.1. Temperature dependence of permittivity

The permittivity (Fig. 5b) was investigated for BTO_3 (Fig. 5a) and $BTSO_3$:2Er) samples over a wide temperature range (−50 to 200 °C) and a frequency range (10^2–10^5 Hz). As a general description, ε' for both samples exhibits high values in the low-frequency region, followed by a significant decrease at high frequencies, in agreement with the result reported for the compounds based relaxor ferroelectric materials [12, 20]. Further, the decrease in permittivity with frequency increase is commonly due to decrease in the total polarization components, i.e., space charge, dipolar, ionic, and atomic polarization. The last two polarizations are excluded from further discussion because their mechanisms are determined at very high frequencies ($> 10^{14}$ Hz) out of our frequency window. In Fig. 5a, ε' of BTO_3 shows three successive relaxation peaks corresponding to three structural transitions. The first is the sharpest and highest intensity peak whose maximum is determined at 125 °C, revealing the tetragonal-cubic phase transition temperature, i.e. the Curie temperature (T_C) [31]. The second is a relatively broad and low-intensity peak, determined at 30 °C, that specifies tetragonal-orthorhombic phase transition temperature (T_{T-O}), while the last one is a weaker relaxation peak whose maximum positioned at −35 °C corresponds to orthorhombic-rhombohedral phase transition temperature (T_{O-R}), as shown in Table III. These transitions have been typically found for all classical ferroelectric materials [32].

TABLE III

Phase transition temperatures for BTO_3 and $BTSO_3$:2Er

Sample	Phase Transition Temperatures [°C]			
	T_{O-R}	T_{T-O}	T_C (T_{C-T})	$> T_C$
BTO_3	−35	30	125	ND*
$BTSO_3$: 2Er	ND*	−6	100	174

*non-detected

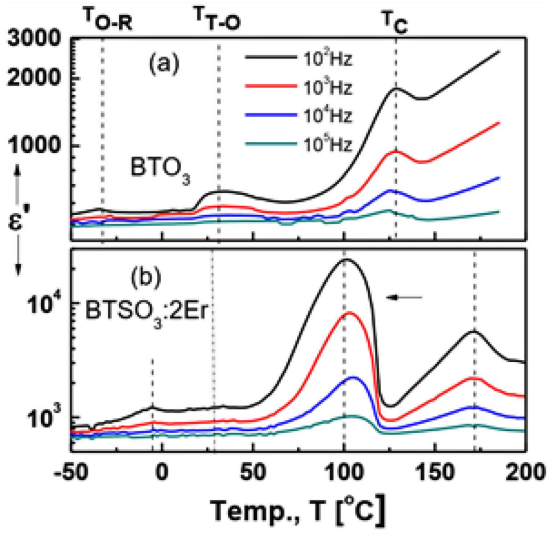

Fig. 5. Temperature dependence of permittivity (ε') at different frequencies for BTO_3 (a) and $BTSO_3$:2Er (b), sintered in air for 4 h at 1050 °C.

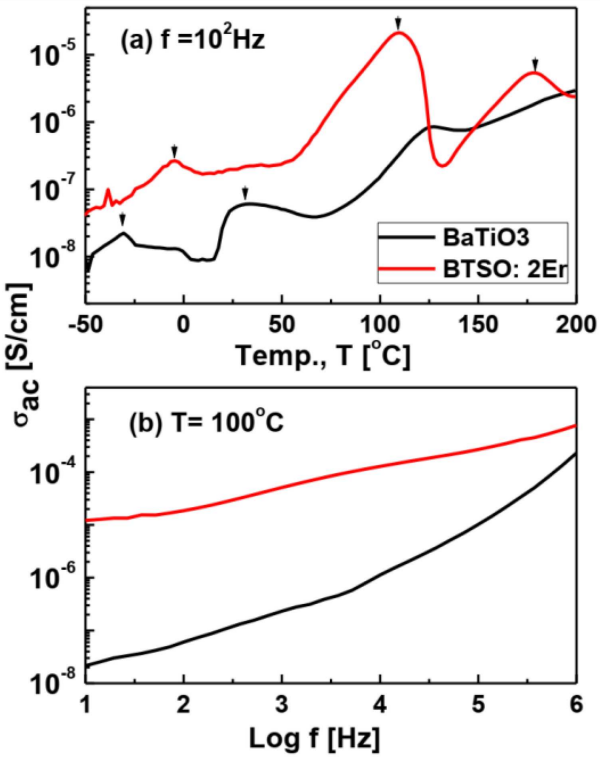

Fig. 6. Temperature (a) and frequency (b) dependence of AC conductivity (σ_{AC}) for BTO_3 (a) and $BTSO_3$: 2Er (b), sintered in air for 4 h at 1050 °C. The arrows indicate the phase transition temperatures.

For $BTSO_3$:2Er sample (Fig. 5b), the shape of ε' curves significantly changed and the phase transition temperatures shifted to lower values. Similar behavior has been reported previously upon the incorporation of Sn ions or/and addition of more than 2 mol.% Er into the stoichiometric BTO_3 [33, 34]. Therefore, Er-doped samples reported no changes in T_C when the concentration of Er ions is lower than 2 mol%. As a result, one may attribute the changes occurring in T_C of $BTSO_3$:2Er sample to the presence of Sn^{4+} ions instead of less effective Er^{3+} ions at low concentrations.

Accordingly, doping with Sn^{4+} results in a remarkable permittivity increase as compared to that reported for pure BTO_3 sample, i.e., it is 1151 at room temperature and 24221 at T_C. This reveals enhanced dielectric properties upon doping BTO_3 with Sn^{4+} ions. The degree of enhancement is larger than those reported for $BaTO_3$ doped with other ions, i.e., Co^{2+}, Bi^{+2}, La/Mn, and Y^{3+}/Nb^{5+} [35–39]. The possible reasons for that would be explained based on a specific amount of space charge sites produced inside the grain boundaries and domain walls. Therefore, the space charge itself creates an opposite electric field hindering the polarization that originates from movements of domain walls and grain boundaries. However, as the densification of $BaTO_3$ is increased, the space-charge fields would be easily reduced by space charge of the surrounding grains. Thus, the domain walls become quite free in denser ceramics, causing a polarization increase that results in a considerable permittivity increase. Another reason may come from the large bond length in the case of Er–O and Sn–O than Ti–O.

Furthermore, ε' of $BTSO_3$:2Er sample exhibits an unexpected relaxation peak whose maximum is positioned at a temperature higher than T_C ($\sim$ 174 °C). Less attention has been paid to discuss the possible reason for such a peak and therefore it is still an open point for future discussion. According to best of our knowledge, we suggest that the orientation polarization of aggregated SnO_2 inside the ceramic whose traces appeared in XRD analysis (Fig. 1a), is responsible for such a peak. It can also be noticed from Fig. 5b that T_C of doped samples shifts to higher temperatures with increasing frequency which may reveal the relaxor ferroelectrics [7, 8].

3.2.2. Temperature and frequency dependence of conductivity

To investigate the relation between the observed relaxation peaks and transportation of free charge carriers through the crystalline lattice, AC conductivity (σ_{AC}) for both BTO_3 and $BTSO_3$:2Er samples is studied at first as a function of temperature at 10^2 Hz (Fig. 6a) and then as a function of frequency at 100 °C (Fig. 6b). In Fig. 6a, σ_{AC} for both samples starts to slightly increase with increasing temperature and then shows anomalous behavior near the structure transition temperatures. Thus, it exhibits also three pronounced relaxation peaks confirming the phase transition feature for the investigated samples. It can also be noticed that a peak position shifts to higher values for $BTSO_3$:2Er sample. The conduction at temperatures below T_C, within the tetragonal ferroelectric may originate from the presence of impurities or defects. Oxygen vacancies as most mobile ionic defects in

perovskite could be responsible for the conduction process [4]. At a temperature higher than T_C, within the cubic paraelectric phase, the electrical conduction could be due to thermally activated ionic hopping of oxygen vacancies in $BTSO_3$:2Er.

On the other side, the frequency-dependent conductivity (Fig. 6b) for both samples displays an increase with a frequency increase, obeying the universal power-law $A\omega^s$ [41, 42]. This arises from the long-range movements and alignments of free charge carriers towards the electric field, resulting in a net flow of charge through samples. The conductivity value of $BTSO_3$:2Er is $\sim 10^3$ times higher than that for barium titanate sample, due to formation of excess oxygen vacancies.

4. Conclusion

Nano-powdered pure and Sn^{4+}/Er^{3+} co-doped BTO_3 ceramics have been successfully synthesized using the modified sol–gel method. The obtained gel converted to crystalline tetragonal powder upon annealing in air at 1050 °C for 4 h. Upon co-doping with Sn^{4+}/Er^{3+} ions, microstructure and dielectric properties significantly changed as follows:

1. Grains became denser and their sizes decreased from 64 to 57.11 nm.
2. The Curie temperature (T_C) shifted from 125 to 103 °C.
3. The permittivity of $BTSO_3$:2Er sample increased to become approximately ten times greater than that of pure BTO_3.
4. AC conductivity value was found to be $\sim 10^3$ times higher than that for pure BTO_3, leading to possibility of using $BTSO_3$:2Er in the field of electrical capacitor fabrication.
5. An unexpected relaxation peak whose maximum was positioned beyond T_C(174 °C) in the permittivity and AC conductivity spectra. It may have originated from the orientation polarization of aggregated SnO_2 inside the ceramic.

Acknowledgments

Providing financial support of this work under Imhotep project 2018–2020 (grant No. 39521QE). A special thanks to National Research Centre, Dokki, and Giza for the laboratory facilities and continual encouragement. The authors extend the thankfulness to the ministries of Europe and Foreign Affairs (MEAE) and Higher Education Research and Innovation (MESRI) and in France Program Hubert Curien (PHC-Imhotep No. 39521QE) as a participating in financial support and Imhotep project 2018–2020.

The authors would like to express their special thanks of gratitude to Professors: A. Lahmar, M. El Marssi, and A. Zeinert, LPMC, Université de Picardie Jules Verne, Amiens, France, for giving them the opportunity to measure the dielectric properties of the samples.

References

[1] R. Asiaie, W. Zhu, S. Ak, P. Dutta, *Chem. Mater.* **8**, 226 (1996).

[2] X. Yang, D. Li, Z. Ren, et al., *RSC Adv.* **6**, 75422 (2016).

[3] T. Lee, C. Huang, C. Chang, I.-Kuan Cheng, C.-Li Hu, C.-Te Lee, M. Fujimoto, *J. Mater. Res.* **27**, 2495 (2012).

[4] H. Dah, I. Chironi, I. Karatchevtseva, G. Triani, C. Sorrel, *Adv. Appl. Ceram.* **111**, 149 (2012).

[5] G. Samara, *J. Phys. Condens. Matter* **15**, R367 (2003).

[6] F. Jona, G. Shirane, *Ferroelectric Crystals*, Pergamon Press, Oxford (UK) 1963.

[7] Y. Liu, R. Withers, B. Nguyen, K. Elliott, *Appl. Phys. Lett.* **91**, 152907 (2007).

[8] G. Smolensky, V. Isupov, *Dokl. Akad. Nauk SSSR* **96**, 53 (1954).

[9] G. Haertling, *J. Am. Ceram. Soc.* **82**, 797 (1999).

[10] X. Wei, X. Yao, *Mater. Sci. Eng. B* **137**, 184 (2007).

[11] Y. Leyet, R. Peña, Y. Zulueta, F. Guerrero, J. Anglada-Rivera, Y. Romaguera, J. Pérez de la Cruz, *Mater. Sci. Eng. B* **177**, 832 (2012).

[12] Y. Tsur, T. Dunbar, C. Randall, *J. Electroceram.* **7**, 25 (2001).

[13] M.T. Buscaglia, M. Viviani, V. Buscaglia, C. Bottino, P. Nanni, *J. Am. Ceram. Soc.* **85**, 1569 (2002).

[14] J. Hwang, Y. Han, *J. Appl. Phys.* **40**, 676 (2001).

[15] S. Singh, P. Singh, O. Parkash, D. Kumar, *J. Alloys Comp.* **493**, 522 (2010).

[16] Y.A. Zulueta, F. Guerrero, Y. Leyet, J. Anglada-Rivera, R.L. González-Romero, J. Meléndez, *J. Phys. Status Solidi B* **252**, 508 (2015).

[17] P. Harold, E. Leroy, *X-ray Diffraction Procedure: For Polycrystalline and Amorphous Materials* Wiley, New York 1974.

[18] E. Antonelli, M. Letonturier, J.C. Mepeko, *J. Eur. Ceram. Soc.* **29**, 1449 (2009).

[19] T. Mandal, *J. Mater. Lett.* **61**, 850 (2007).

[20] K. Uchino, E. Sadanaga, T. Hirose, *J. Am. Ceram. Soc.* **72**, 1555 (1989).

[21] K. Fukai, K. Hidaka, M. Aoki, K. Abe, *Ceram. Int.* **16**, 285 (1990).

[22] T. Yamamoto, K. Urabe, H. Banno, *Jpn. J. Appl. Phys.* **32**, 4272 (1993).

[23] L. Songwei, I. Burtrand, M. Larry, *J. Mater. Res. Bull.* **35**, 1303 (2000).

[24] S. Chang, W. Liao, C. Ciou, J. Lee, C. Li, *J. Coll. Interface Sci.* **329**, 300 (2009).

[25] G. Chen, Y. Liu, Z. Zhang, B. Aghahadi, G. Somesfalean, Q. Sunand, F. Wang, *Chem. Phys. Lett.* **448**, 127 (2007).

[26] M. Cernea, *J. Optoelectron. Adv. Mater.* **7**, 3015 (2005).

[27] H. Zhang, C. Kam, Y. Zhou, X. Han, Y. Lam, Y. Chan, K. Pita, *Mater. Chem. Phys.* **63**, 174 (2000).

[28] R. Ganapathi, K. Chidambara, R. Lakshmi, V. Nirupama, *J. Mater. Sci. Mater. Electron.* **30**, (2019).

[29] T. Supin, J. Milne, *J. Non-Cryst. Solids* **351**, 976 (2005).

[30] K. Kao, in: *Dielectric Phenomena in Solids, Ferroelectrics, Piezoelectrics and Pyroelectrics*, 1st ed., Elsevier, 2004, p. 213 .

[31] A. Ayesh, R. Abdel-Rahem, *Bull. Mater. Sci.* **33**, 589 (2010).

[32] S. Upadhyay, V. Reddy, P. Bag, R. Rawat, S. Gupta, A. Gupta, *Appl. Phys. Lett.* **105**, 112907 (2014).

[33] S. Marković, M. Mitrić, N. Cvjetićanin, D. Uskokovic, *Mater. Sci. Forum* **518**, 241 (2006).

[34] V. Shvartsman, J. Dec, Z. Xu, J. Banys, P. Keburis, W. Kleemann, *Phase Transit.* **81**, 1013 (2008).

[35] Z. Zhuang, M. Hamer, D. Smyth, *Mater. Res. Bull.* **22**, 1329 (1987).

[36] P. Krishna, D. Pandey, V. Tiwari, R. Chakravathy, B. Dasannacharya, *Appl. Phys. Lett.* **62**, (1993).

[37] S. Lee, C. Randall, *Appl. Phys. Lett.* **92**, 111904 (2008).

[38] L. Zhang, O. Thakur, A. Feteira, G. Keith, A. Mould, *Appl. Phys. Lett.* **90**,142914 (2007).

[39] L. Da-Yong, G. Xiang-Lu, W. Shan, *Results Phys.* **12**, 585 (2019).

[40] K. Gschneider, L. Eyring, in: *Handbook on the Physics and Chemistry of Rare Earths*, North Holland, Amsterdam 1980.

[41] A. Jonscher, *Thin Solid Films* **100**, 329 (1983).

[42] A. Jonscher, *Nature* **267**, 673 (1977).